THE JOURNAL OF PHYSICAL CHEMISTRY C

pubs.acs.org/JPCC Article

Mechanical Properties and Failure Envelope of Kerogen Matrix by Molecular Dynamics Simulations

Tianhao Wu and Abbas Firoozabadi*

Cite This: J. Phys. Chem. C 2020, 124, 2289−2294 Read Online

ACCESS | Metrics & More | Article Recommendations | Supporting Information

ABSTRACT: Shale gas has become a major source of gas supply in the United States and is becoming increasingly important worldwide. The key technique for the development is hydraulic fracturing in horizontal wells. Kerogen is the main component of organic matter in shale. It may be the spot of fracture initiation due to its weaker mechanical properties. The measurement of the mechanical properties and failure envelope of kerogen may be a challenge due to small-size kerogen aggregates immersed in shale rocks. In this work, we propose a practical scheme based on molecular dynamics simulations to estimate the elastic and relevant mechanical properties of kerogen for fracturing, including Young's modulus, Poisson's ratio, compressive and tensile strengths, as well as the parameters of the Mohr−Coulomb failure criterion. This work sets the stage to obtain basic kerogen parameters for the simulation of fracturing in shale rocks.

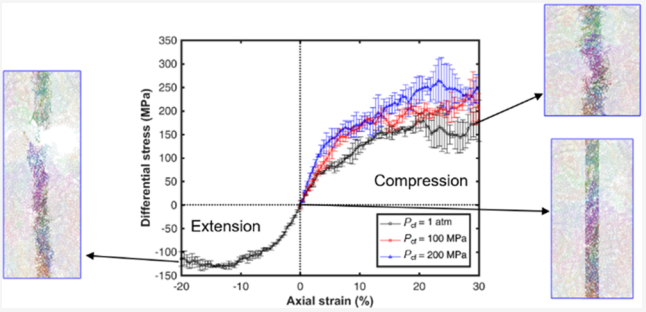

INTRODUCTION

Shale gas from organic-rich shale formations has changed the worldwide energy landscape.[1,2] The development of shale gas formation is through multistage hydraulic fracturing in horizontal wells.[3] The stewardship of the environment in hydrocarbon energy production can be facilitated by effective fracturing techniques and application of nonaqueous fracturing fluids. Fracturing design is a critical step for shale reservoir resource development through accurate fracturing simulations.[3,4] Fundamental knowledge of fracturing mechanisms is essential to improve effectiveness. The mechanical properties of the rock can be affected by the fracturing fluids, but the mechanisms are largely unknown.[5−12]

The stress condition of a rock element can be described by Mohr's circle. Failure envelope can be described through the locus of a series of Mohr's circles that represent the shear and normal stresses at critical failure conditions. The failure envelope is often used as the criterion of fracture initiation and propagation in reservoir simulations of fracturing. The mechanical properties and failure envelope of shale media are generally measured by the uniaxial/triaxial compression tests and Brazilian tensile tests suggested by the International Society for Rock Mechanics (ISRM) and the American Society for Testing and Materials (ASTM).[13−19] However, many subtle effects and mechanisms cannot be accurately investigated by macroscopic methods because of the heterogeneity in the rock.

Shale rock is comprised of two distinct media, organic and inorganic matters, which have different chemical and mechanical properties. Fracturing fluids may have different effects on each constituent in shale, which may lead to complicated macroscopic behavior. To understand the microscopic mechanisms that control the mechanical properties, the nanomechanical measurements, including quasi-static nanoindentation and modulus mapping, are often conducted on the mineral grains at the nanoscale.[20−22] Recent measurements by nanoindentation on shale provide evidence of a significant difference in Young's modulus from different minerals in the same sample.[20] Measurements on the effect of different fracturing fluids on mechanical properties at the nanoscale are major challenges. In this respect, nanoscale simulations may provide valuable information on investigating the mechanisms. The complicated behavior of fracture initiation and propagation at the meso/macroscale can be simulated based on the properties from microscopic simulations. However, microscopic simulations are generally based on noncontinuum theory.

Molecular dynamics (MD) simulations of mechanical properties have been performed recently for some of the minerals in shale, including the tensile failure of illite, silica, and porous carbon, as well as clay-porous carbon composite material.[23−26] In inorganic matters, water may lead to clay swelling, which affects the overall properties of the rock.[27,28] Kerogen is the predominant component of organic matter in most shale formations,[29,30] and representative molecular structures have been constructed based on the properties from geochemical

Received: October 13, 2019
Revised: December 23, 2019
Published: January 8, 2020

https://dx.doi.org/10.1021/acs.jpcc.9b09639
J. Phys. Chem. C 2020, 124, 2289−2294

experiments.[31,32] As a mechanically weaker component in shale, kerogen aggregates can serve as the spot for fracture initiation. Kerogen aggregates are dispersed in shale media in the submillimeter range. It is not practical to accurately and systematically perform the mechanical tests on very small kerogen pieces to determine the failure envelope. In this regard, MD simulation can be a natural approach. This is the main objective of this work.

We propose a practical scheme to construct the link between microscale and macroscale for kerogen medium to obtain the mechanical properties and failure envelope based on MD simulations. We obtain the stress−strain curves from the strain-induced processes of compression and extension followed by mechanical properties, including Young's modulus, Poisson's ratio, compressive strength, and tensile strength, as well as the parameters for the Mohr−Coulomb failure criterion.

KEROGEN MATRIX CREATION, COMPRESSION, AND EXTENSION

Because of different depositional environments and geological processes, the kerogens possess different molecular structures, which may result in different mechanical properties. We use three types of kerogen macromolecules in this study (see Figure S1). The kerogen macromolecule units are adapted from Ungerer et al.,[32] which reproduce the elemental and functional data of kerogen including the H/C, O/C, and N/C ratios, average aromaticity, and average size of the aromatic unit. The type I macromolecule ($C_{251}H_{385}O_{13}N_7S_3$) represents the kerogen deposited in anoxic lacustrine environments and is relevant for the shale oil reservoirs in the Green River Basin. The type II kerogen macromolecule ($C_{252}H_{294}O_{24}N_6S_3$) is representative of the oil-prone organic matter deposited in anoxic marine environments, which is considered as the most common source of conventional hydrocarbon resources. We select the immature kerogen to construct the matrix.[32] The type III macromolecule ($C_{233}H_{204}O_{27}N_4$) is representative of the kerogen from organic-rich shales and coals deposited in post-Jurassic deltaic environments. We create three different kerogen matrices with about the same size consisting of representative macromolecules (see Figures S2−S6). We select the type III as an example to demonstrate the method for matrix construction as well as compression and extension. Detailed procedures of the simulations are presented in the Supporting Information.

To obtain the mechanical properties, we perform a quasi-static strain-driven mechanical process by applying a series of small compressive and tensile strains and calculate the resulting stress (Figure 1). A series of displacements are applied in the z direction of the box, and all the atoms are relocated proportionally. The displacements of each stage are set to 0.5 Å. In the Supporting Information, we use a smaller displacement of 0.25 Å and show the results to be close to the 0.5 Å displacement. The temperature is maintained by using the Nose−Hoover thermostat at 298.15 K. The barostat is applied to maintain the confining pressure in the x and y directions. The stress in the z direction is varied and monitored. There are 70 and 50 stages for compression and extension, respectively. Each stress condition is repeated from three different initial configurations. The method is validated based on the simulation of illite (see Supporting Information).

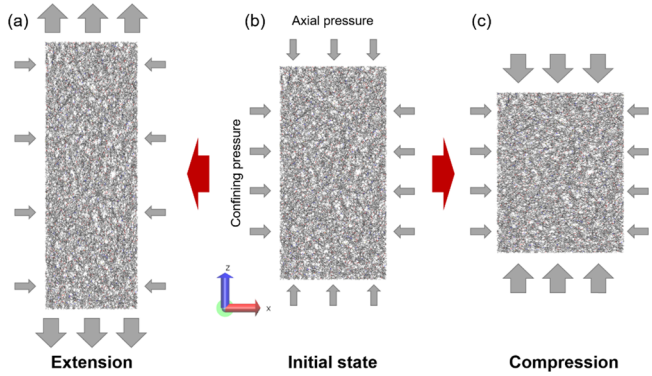

Figure 1. Sketch of kerogen compression and extension. The simulations of kerogen (c) compression and (a) extension start from the same (b) initial structure at a given confining pressure. The axial pressure is set the same as the confining pressure at the initial state. The confining pressure in the x and y directions are kept constant and equal to the initial axial pressure.

FAILURE MODES

We first perform compression in the three types of kerogen matrices at three different confining pressures. The differential stress ($\Delta\sigma$), axial strain (ε_z), and bulk strain (ε_V) are defined as

$$\Delta\sigma = \sigma_z - \sigma_{x,y} = P_{zz} - P_{cf}$$

$$\varepsilon_z = \frac{\Delta z}{L_z(0)}$$

$$\varepsilon_v = \frac{\Delta V}{V(0)}$$

where σ_z and $\sigma_{x,y}$ are the stress in the z and x, y directions, P_{cf} is the confining pressure, and $L_z(0)$ and $V(0)$ are the initial length in the z direction and the initial volume, respectively. The compressive stress and strain are defined as positive, while the tensile stress and strain are defined as negative.

The stress−strain relationships of type III kerogen in compression and extension at three different confining pressures are presented in Figure 2. The results of the other two types of kerogen are provided in the Supporting Information (see Figures S8−S10). The kerogen matrix shows a pronounced ductile behavior. We do not find a brittle rupture either in compression or in extension. In compression, the stress−strain curve can be divided roughly into three regions. In each kerogen matrix, the start is with an elastic region where the differential stress has a linear relationship with the axial strain and bulk strain. The slope of the stress−strain curve in the elastic region increases with confining pressure. In the second region, the slope of $\Delta\sigma$ versus ε_z starts to change and has a nonlinear behavior at which the kerogen starts to yield and shows a plastic behavior. Kerogen matrices undergo the nonrecoverable deformation, and microcracks may initiate in this region. These mechanisms lead to a nonmonotonic relationship in terms of the bulk strain. Finally, the stress−strain curves have significant fluctuations at high axial strain (>∼15%), where the material failure (rupture) occurs. In terms of bulk strain, a disordered relationship is observed in compression (see Figure 2a,c). In this region, we define the critical stress for failure at the highest axial stress. Based on the results, the critical stress increases with confining pressure. The other two kerogen matrices have similar behavior (see Figures S8−S10).

https://dx.doi.org/10.1021/acs.jpcc.9b09639
J. Phys. Chem. C 2020, 124, 2289−2294

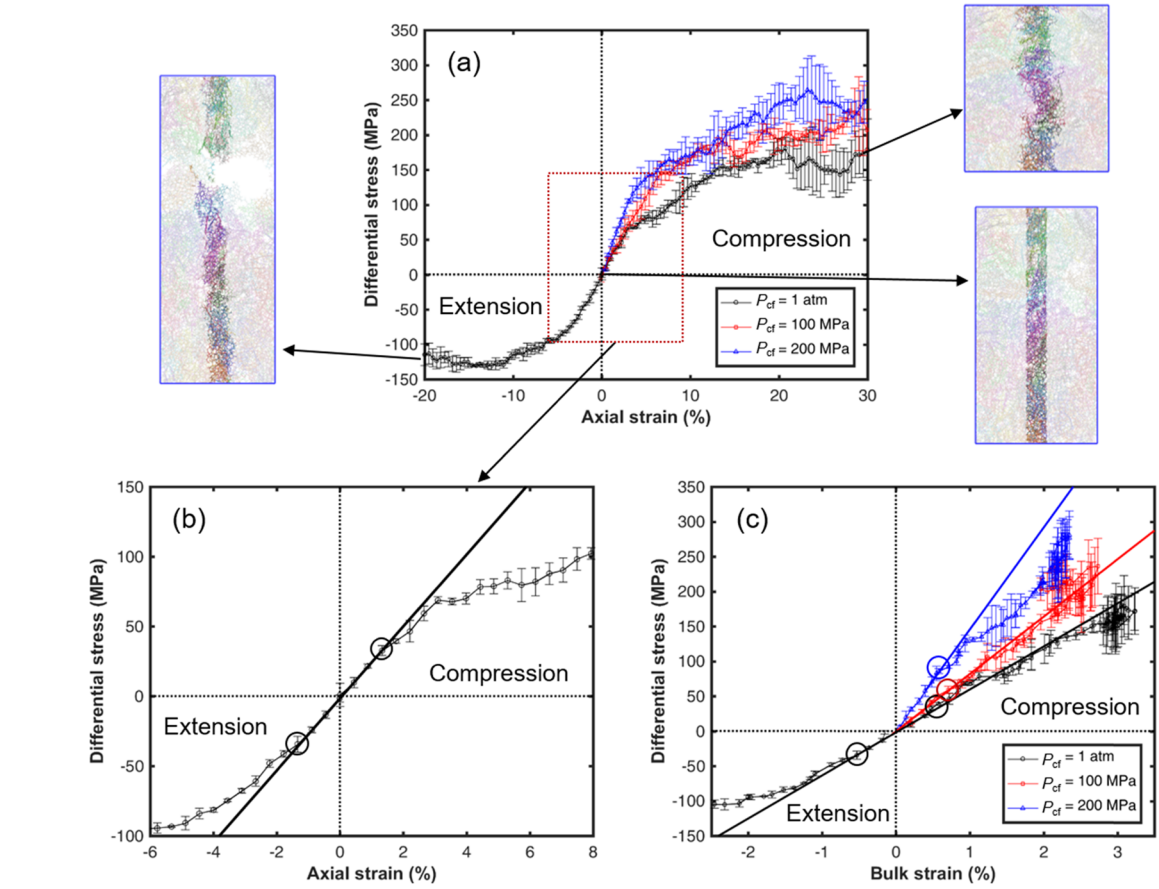

Figure 2. Stress−strain relationships of type III kerogen. (a) Differential stress as a function of axial strain. Compression is simulated at three different confining pressures; the extension is performed at 1 atm. The coordinates of the atoms are tracked from the initial 1 nm-thick slice. Each macromolecule unit is marked with an exclusive color. (b) Enlarged stress−strain relationship of the early region of compression and extension (red box in (a)) at a confining pressure of 1 atm. (c) Differential stress as a function of bulk strain. The lines in (b) and (c) are fitted with the points in the linear region. The circles are the yield points where the kerogen turns to plastic from elastic. The error bars are based on three different simulations.

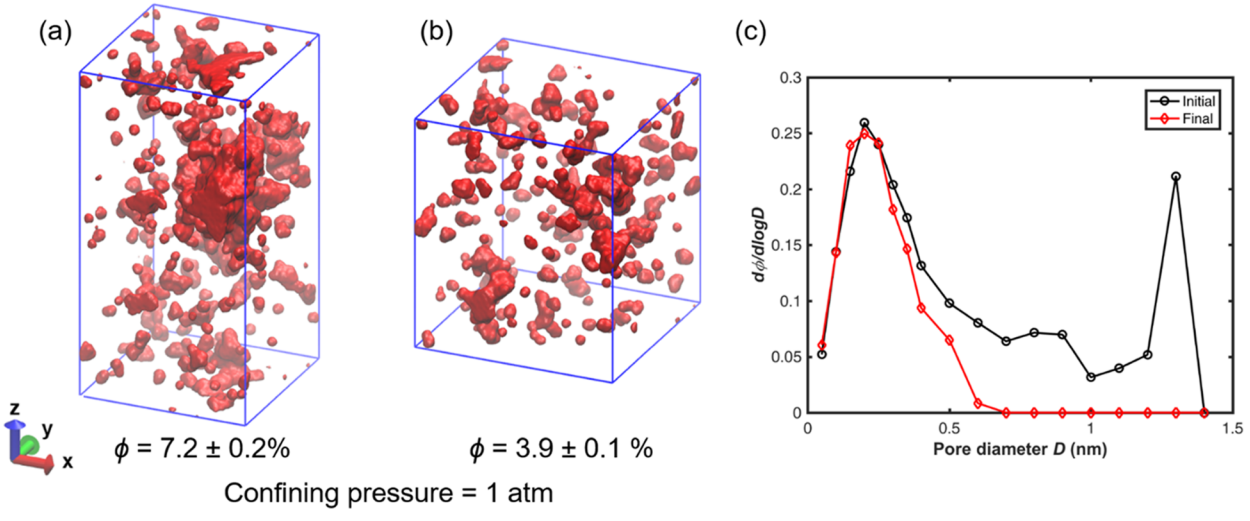

Figure 3. Pore structure changes in compression (type III kerogen). (a) Pore structure at the initial state (ε_z = 0%). (b) Pore structure at the final state of compression (ε_z = 30%). (c) Pore size distributions corresponding to the structures in (a) and (b).

The tensile stress−strain curve has three regions, similar to compression. It starts with a linear behavior followed by plastic deformation and finally breaks at a high axial strain. When we combine the stress−strain curve of extension and compression, the linear region has the same slope (see Figure 2b).

To demonstrate the internal dislocation of the atoms at failure, we trace the coordinates of the atoms in a 1 nm-thick slab from the initial structure. The final positions of these atoms after compression and extension are presented in Figure 2 and Figure S11. In compression, there is a clear shear failure. The pore

https://dx.doi.org/10.1021/acs.jpcc.9b09639
J. Phys. Chem. C 2020, 124, 2289−2294

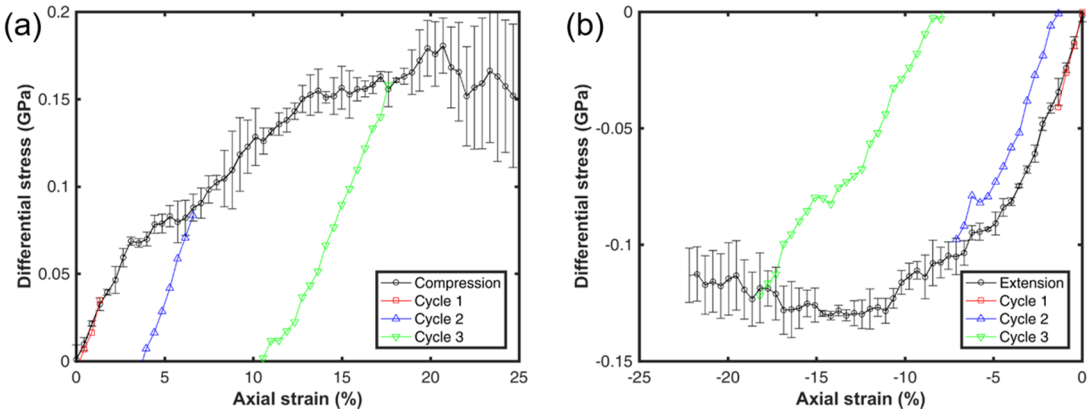

Figure 4. Stress−strain relationships of loading−unloading cycles in compression and extension at a confining pressure of 1 atm in type III kerogen. (a) Compression. The three unloading cycles start from ε_z = 1.3, 6.2, and 17.0%. (b) Extension. The three unloading cycles start from ε_z = −1.3, −6.2, and −17.0%.

Table 1. Mechanical Properties of Three Different Types of Kerogen Matrix from MD Simulations and Experimental Data of Young's Modulus from the Literature

mechanical properties	confining pressure	type I	type II	type III	experimental data[e]
Young's modulus (GPa)	1 atm	1.5 ± 0.5	2.2 ± 0.3	2.6 ± 0.4	10[a]
	100 MPa	1.7 ± 0.2	2.7 ± 0.1	2.9 ± 0.2	6[b]
	200 MPa	2.0 ± 0.3	2.9 ± 0.2	3.6 ± 0.5	10.5[c]
					3.2−29.1[d]
Poisson's ratio	1 atm	0.24 ± 0.03	0.36 ± 0.02	0.32 ± 0.06	
	100 MPa	0.37 ± 0.02	0.40 ± 0.01	0.37 ± 0.05	
	200 MPa	0.40 ± 0.04	0.41 ± 0.02	0.42 ± 0.03	
compressive strength (MPa)	1 atm	100.1	186.1	166.3	
tensile strength (MPa)	1 atm	72.9	129.2	133.3	
cohesion (MPa)		42.8	79.2	78.5	
friction coefficient		0.161	0.191	0.153	

[a]Wilkinson et al.[21] [b]Goodarzi et al.[22] [c]Zhao et al.[20] [d]Emmanuel et al.[33] [e]The confining pressures of these experiments are not specified in the references.

structure has changed significantly (Figure 3 and Figure S12). The pores larger than 0.7 nm disappear completely while the smaller pores persist because of the molecular structure of type III kerogen. In the extension region, the fracture initiates from the relatively large pores, and the atoms in the half bottom have a minor lateral dislocation (see Figure 2a).

We performed three loading−unloading cycles in different ranges of axial strain (see Figure 4) to investigate the elastic and plastic regions. The results show that the kerogen matrix is fully elastic below the axial strain of 1.3% where the matrix can fully recover in both compression and extension. Cycle 2 starts from the middle of the plastic region, and cycle 3 starts from the failure region. In cycles 2 and 3, only part of the strain is recoverable. The slopes of the unloading curves are close, which implies that the elasticity persists to some extent.

■ ELASTIC PROPERTIES AND FAILURE ENVELOPE

The elastic properties are based on the results in the linear region, including Young's modulus (E) and Poisson's ratio (ν). These two properties can be obtained from the simulations directly

$$E = \frac{d\sigma_z}{d\varepsilon_z}$$

$$\nu = -\frac{dx}{dz} = -\frac{dy}{dz}$$

The results of the three kerogen matrices are presented in Table 1. Young's modulus is in the range of 1.5−3.6 GPa, which is of the same order of magnitude as the experimental results from nanoindentation, modulus mapping, and atomic force microscopy (3.2−29.1 GPa).[20−22,33] Compared to other minerals in shale, for example, quartz (50−70 GPa), illite (24−225 GPa), and carbonate (53−56 GPa), kerogen has a much lower Young's modulus than the other minerals in shale.[20−23] In each matrix, Young's modulus increases with confining pressure. Poisson's ratio also increases with confining pressure, but the difference between the three types is not pronounced. The range of Poisson's ratio is from 0.24 to 0.42. It is relatively higher than other minerals, for example, quartz (∼0.08), illite (0.285−0.315), and carbonate (0.29−0.31).[34,35] Poisson's ratio is a key parameter in the estimation of Young's modulus in nanoindentation. Poisson's ratio of kerogen has not been measured to the best of our knowledge. A value of ∼0.25 has been reported based on an indirect method from the knowledge of Young's modulus, shear modulus, and bulk modulus from MD simulations.[31]

Based on our simulations, one can obtain other mechanical properties such as the critical stress in compression and extension at the confining pressure of 1 atm, and the uniaxial compressive strength and tensile strength. The conditions in our simulations are similar to experiments. The results presented in Table 1 reveal that type II kerogen has the highest compressive strength, followed by type III and then type I.

https://dx.doi.org/10.1021/acs.jpcc.9b09639
J. Phys. Chem. C 2020, 124, 2289−2294

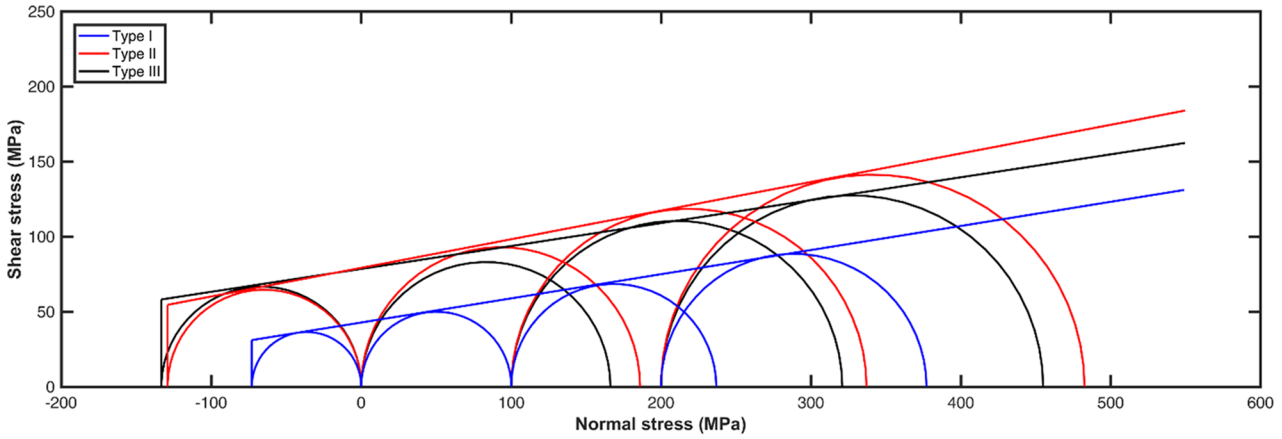

Figure 5. Failure envelope of three different types of kerogen matrix. Mohr's circles of compression and extension are presented for the three samples. The lines of the shear failure region are fitted by the Mohr−Coulomb failure criterion. The tensile strength criterion is applied for the tensile failure.

Mohr's circles of the stress states, which describe the imminent shear failure in each matrix at the three confining pressures, are presented in Figure 5, and an illustration of the method is presented in Figure S15. The Mohr−Coulomb failure criterion is applied for the compression region, which is given as[36]

$$\tau = \sigma \tan(\varphi) + c = \mu\sigma + c$$

where τ is the shear stress, σ is the normal stress, φ is the angle of internal friction, c is the cohesion, and μ is the internal friction coefficient. For the tensile failure, we use the tensile strength criterion, where the tensile failure occurs at

$$\sigma'_3 \leq -T_c$$

where σ'_3 is the minimum principal effective stress and T_c is the tensile strength. The complete failure envelopes for the three types of kerogen are presented in Figure 5. The friction coefficient of kerogen is much lower than that of typical brittle materials, while the cohesion is much higher.[3] Its tensile strength is also much higher than that of the brittle rocks.[37]

CONCLUSIONS

The mechanical properties and failure envelope of kerogen are obtained from MD simulations. Based on our results, the following conclusions are drawn:

(1) The stress−strain curves, both in compression and extension, have three regions. They start with a linear behavior followed by plastic deformation and finally break at a high axial strain;
(2) Kerogen has a much lower Young's modulus and a slightly higher Poisson's ratio than other minerals in shale. Its compressive strength is much lower and its tensile strength is higher than those of the brittle rocks;
(3) The Mohr−Coulomb failure criterion and tensile strength criterion based on molecular simulations can describe the failure envelope of the kerogen matrix, which has the same features as that from the macroscopic perspective.

The results of kerogen mechanical properties from MD simulations provide the essential parameters for mesoscopic and macroscopic simulations and provide a critical link from the molecular scale to meso/macroscale. Since it is likely that the fractures are initiated from kerogen, one can get the basic parameters from molecular simulations.

ASSOCIATED CONTENT

Supporting Information

The Supporting Information is available free of charge at https://pubs.acs.org/doi/10.1021/acs.jpcc.9b09639.

Details and additional results of kerogen matrix creation, compression, and extension by molecular dynamics simulation, including procedures, method validation, relevant properties of the created matrices, and the results of types I and II kerogen matrices (PDF)

AUTHOR INFORMATION

Corresponding Author

Abbas Firoozabadi − *Reservoir Engineering Research Institute, Palo Alto, California 94301, United States;* orcid.org/0000-0001-6102-9534; Email: af@rerinst.org

Other Author

Tianhao Wu − *Reservoir Engineering Research Institute, Palo Alto, California 94301, United States; Chemical and Biomolecular Engineering Department, Rice University, Houston, Texas 77005, United States*

Complete contact information is available at: https://pubs.acs.org/10.1021/acs.jpcc.9b09639

Notes

The authors declare no competing financial interest.

ACKNOWLEDGMENTS

The work was supported by the member companies of the Reservoir Engineering Research Institute (RERI). Their support is appreciated.

REFERENCES

(1) US Energy Information Administration. *Annual Energy Outlook 2019: With Projections to 2050*; https://www.eia.gov/outlooks/aeo/ (accessed January2019).
(2) US Energy Information Administration. *Technically Recoverable Shale Oil and Shale Gas Resources*; https://www.eia.gov/analysis/studies/worldshalegas/ (accessed January 2019).
(3) Li, S.; Zhang, D. How Effective is Carbon Dioxide as an Alternative Fracturing Fluid? *SPE J.* **2019**, *24*, 857−876.
(4) Li, S.; Zhang, D.; Li, X. A New Approach to the Modeling of Hydraulic-Fracturing Treatments in Naturally Fractured Reservoirs. *SPE J.* **2017**, *22*, 1064−1081.

(5) Lyu, Q.; Long, X.; Ranjith, P. G.; Tan, J.; Kang, Y.; Wang, Z. Experimental Investigation on the Mechanical Properties of a Low-Clay Shale with Different Adsorption Times in Sub-/Super-Critical CO_2. *Energy* **2018**, *147*, 1288−1298.
(6) Al-Ameri, W. A.; Abdulraheem, A.; Mahmoud, M. Long-Term Effects of CO_2 Sequestration on Rock Mechanical Properties. *J. Energy Resour. Technol.* **2016**, *138*, No. 012201.
(7) Yin, H.; Zhou, J.; Xian, X.; Jiang, Y.; Lu, Z.; Tan, J.; Liu, G. Experimental Study of the Effects of Sub-and Super-Critical CO_2 Saturation on the Mechanical Characteristics of Organic-Rich Shales. *Energy* **2017**, *132*, 84−95.
(8) Perera, M. S. A.; Ranjith, P. G.; Viete, D. R. Effects of Gaseous and Super-Critical Carbon Dioxide Saturation on the Mechanical Properties of Bituminous Coal from the Southern Sydney Basin. *Appl. Energy* **2013**, *110*, 73−81.
(9) Lu, Y.; Chen, X.; Tang, J.; Li, H.; Zhou, L.; Han, S.; Ge, Z.; Xia, B.; Shen, H.; Zhang, J. Relationship between Pore Structure and Mechanical Properties of Shale on Supercritical Carbon Dioxide Saturation. *Energy* **2019**, *172*, 270−285.
(10) Wang, S.; Liu, K.; Han, J.; Ling, K.; Wang, H.; Jia, B. Investigation of Properties Alternation During Super-Critical CO_2 Injection in Shale. *Applied Sciences* **2019**, *9*, 1686.
(11) Sun, Z.; Espinoza, D. N.; Balhoff, M. T.; Dewers, T. A. Discrete Element Modeling of Micro-Scratch Tests: Investigation of Mechanisms of CO_2 Alteration in Reservoir Rocks. *Rock Mechanics and Rock Engineering* **2017**, *50*, 3337−3348.
(12) Sun, Z.; Espinoza, D. N.; Balhoff, M. T. Discrete Element Modeling of Indentation Tests to Investigate Mechanisms of CO_2-Related Chemomechanical Rock Alteration. *Journal of Geophysical Research: Solid Earth* **2016**, *121*, 7867−7881.
(13) Bienniawski, Z. T.; Hawkes, I. Suggested Methods for Determining Tensile Strength of Rock Materials. *Int. J. Rock Mech. Min. Sci. Geomech. Abstr.* **1978**, *15*, 99−103.
(14) Kovari, K.; Tisa, A.; Einstein, H.; Franklin, J. Suggested Methods for Determining the Strength of Rock Materials in Triaxial Compression: Revised Version. *Int. J. Rock Mech. Min. Sci. Geomech. Abstr.* **1983**, *20*, 285−290.
(15) ASTM. *D3967-08. Standard Test Method for Splitting Tensile Strength of Intact Rock Core Specimens*; ASTM International: Weste Conshohocken, USA 2008.
(16) ASTM. Standard Test Method for Compressive Strength and Elastic Moduli of Intact Rock Core Specimens under Varying States of Stress and Temperatures. D7012-10. *ASTM International,* West Conshohocken, USA 2010.
(17) Dewhurst, D. N.; Hennig, A. L. Geomechanical Properties Related to Top Seal Leakage in the Carnarvon Basin, Northwest Shelf, Australia. *Pet. Geosci.* **2003**, *9*, 255−263.
(18) Islam, M. A.; Skalle, P. An Experimental Investigation of Shale Mechanical Properties through Drained and Undrained Test Mechanisms. *Rock Mech. Rock Eng.* **2013**, *46*, 1391−1413.
(19) Josh, M.; Esteban, L.; Delle Piane, C.; Sarout, J.; Dewhurst, D. N.; Clennell, M. B. Laboratory Characterisation of Shale Properties. *J. Pet. Sci. Eng.* **2012**, *88-89*, 107−124.
(20) Zhao, J.; Zhang, D.; Wu, T.; Tang, H.; Xuan, Q.; Jiang, Z.; Dai, C. Multiscale Approach for Mechanical Characterization of Organic-Rich Shale and Its Application. *Int. J. Geomech.* **2019**, *19*, 04018180.
(21) Wilkinson, T. M.; Zargari, S.; Prasad, M.; Packard, C. E. Optimizing Nano-Dynamic Mechanical Analysis for High-Resolution, Elastic Modulus Mapping in Organic-Rich Shales. *J. Mater. Sci.* **2015**, *50*, 1041−1049.
(22) Goodarzi, M.; Rouainia, M.; Aplin, A. C.; Cubillas, P.; de Block, M. Predicting the Elastic Response of Organic-Rich Shale Using Nanoscale Measurements and Homogenisation Methods. *Geophys. Prospect.* **2017**, *65*, 1597−1614.
(23) Hantal, G.; Brochard, L.; Laubie, H.; Ebrahimi, D.; Pellenq, R. J.-M.; Ulm, F.-J.; Coasne, B. Atomic-Scale Modelling of Elastic and Failure Properties of Clays. *Mol. Phys.* **2014**, *112*, 1294−1305.
(24) Brochard, L.; Hantal, G.; Laubie, H.; Ulm, F.-J.; Pellenq, R. J. M. Capturing Material Toughness by Molecular Simulation: Accounting for Large Yielding Effects and Limits. *Int. J. Fract.* **2015**, *194*, 149−167.
(25) Hantal, G.; Brochard, L.; Dias Soeiro Cordeiro, M. N.; Ulm, F. J.; Pellenq, R. J.-M. Surface Chemistry and Atomic-Scale Reconstruction of Kerogen−Silica Composites. *J. Phys. Chem. C* **2014**, *118*, 2429−2438.
(26) Hantal, G.; Brochard, L.; Pellenq, R. J.-M.; Ulm, F.-J.; Coasne, B. Role of Interfaces in Elasticity and Failure of Clay−Organic Nanocomposites: Toughening Upon Interface Weakening? *Langmuir* **2017**, *33*, 11457−11466.
(27) Kadoura, A.; Narayanan Nair, A. K.; Sun, S. Molecular Dynamics Simulations of Carbon Dioxide, Methane, and Their Mixture in Montmorillonite Clay Hydrates. *The Journal of Physical Chemistry C* **2016**, *120*, 12517−12529.
(28) Li, Y.; Narayanan Nair, A. K.; Kadoura, A.; Yang, Y.; Sun, S. Molecular Simulation Study of Montmorillonite in Contact with Water. *Ind. Eng. Chem. Res.* **2018**, *58*, 1396−1403.
(29) Wu, T.; Li, X.; Zhao, J.; Zhang, D. Multiscale Pore Structure and Its Effect on Gas Transport in Organic-Rich Shale. *Water Resour. Res.* **2017**, *53*, 5438−5450.
(30) Wu, T.; Firoozabadi, A. Effect of Microstructural Flexibility on Methane Flow in Kerogen Matrix by Molecular Dynamics Simulations. *The Journal of Physical Chemistry C* **2019**, *123*, 10874−10880.
(31) Bousige, C.; et al. Realistic Molecular Model of Kerogen's Nanostructure. *Nat. Mater.* **2016**, *15*, 576−582.
(32) Ungerer, P.; Collell, J.; Yiannourakou, M. Molecular Modeling of the Volumetric and Thermodynamic Properties of Kerogen: Influence of Organic Type and Maturity. *Energy Fuels* **2015**, *29*, 91−105.
(33) Emmanuel, S.; Eliyahu, M.; Day-Stirrat, R. J.; Hofmann, R.; Macaulay, C. I. Impact of Thermal Maturation on Nano-Scale Elastic Properties of Organic Matter in Shales. *Mar. Pet. Geol.* **2016**, *70*, 175−184.
(34) Wang, Z.; Wang, H.; Cates, M. E. Effective Elastic Properties of Solid Clays. *Geophysics* **2001**, *66*, 428−440.
(35) Ahrens, T. J. *Mineral Physics & Crystallography: A Handbook of Physical Constants*; American Geophysical Union: Washington, DC, USA, 1995; Vol. 2.
(36) Labuz, J. F.; Zang, A. Mohr−Coulomb Failure Criterion. *Rock Mech. Rock Eng.* **2012**, *45*, 975−979.
(37) You, M. Strength Criterion for Rocks under Compressive-Tensile Stresses and Its Application. *J. Rock Mech. Geotech. Eng.* **2015**, *7*, 434−439.

https://dx.doi.org/10.1021/acs.jpcc.9b09639
J. Phys. Chem. C 2020, 124, 2289−2294